MATERIALS CHEMISTRY FRONTIERS

RESEARCH ARTICLE

View Article Online
View Journal | View Issue

Cite this: *Mater. Chem. Front.*, 2025, **9**, 2752

Multicolor 3D afterglow structures with high precision and ultralong lifetimes based on carbazole-doped photocurable resins†

Rui Du,[a] Zhengshuo Wang,[a] Zhipeng Zhao,[a] Huilong Liu,[a] Shouchang Jiao,[a] Yi Wu,[a] Wenhui Li,[a] Hua Yuan,[a] Hanlin Ou *[a] and Dan Ding *[b]

Received 14th May 2025,
Accepted 19th July 2025

DOI: 10.1039/d5qm00369e

rsc.li/frontiers-materials

The majority of current research on organic room-temperature phosphorescence (RTP) materials focuses on film or powder forms, with limited exploration into the fabrication of complex 3D structures with high precision and enhanced RTP properties. Herein, a general strategy is proposed to construct 3D RTP models with precise structures and ultralong lifetimes by micro-doping carbazole-based chromophores into photocurable standard resins (SRs) and combining them with photocurable 3D printing technology. The highly cross-linked and rigid microenvironment formed after the curing of SRs endows the carbazole-doped SRs with a long RTP lifetime of up to 1.8 s. Utilizing digital light processing 3D printing technology, a series of multidimensional RTP models with precise structures and ultralong lifetimes are constructed based on these carbazole-doped SRs. Given the superior tunability of 3D printing blueprints and the excellent RTP properties of the printed models, these multidimensional models demonstrate great application prospects in advanced anti-counterfeiting and encryption applications.

Introduction

Organic room-temperature phosphorescence (RTP) materials have attracted significant attention in diverse fields such as display technologies, information encryption, anti-counterfeiting, organic light-emitting diodes (OLEDs) and bioimaging, owing to their unique advantages including large Stokes shifts, prolonged luminescence lifetimes, and good biocompatibility.[1–8] However, the inherent spin-forbidden nature of singlet-to-triplet transitions typically results in low RTP efficiency.[9–11] Moreover, the susceptibility of long-lived triplet excitons to quenching by environmental factors, such as water and oxygen, presents a significant challenge in achieving persistent and bright phosphorescence emissions.[12–16] To address these limitations, many strategies such as crystal assembly,[17–22] host–guest encapsulation,[23–27] and polymer doping[28–32] have been developed to enhance the intersystem crossing (ISC) efficiency and mitigate triplet exciton quenching in organic RTP materials. Among these strategies, the polymer doping strategy, which capitalizes on the rigid microenvironment created by van der Waals forces and hydrogen bonding interactions within the polymer matrix to suppress non-radiative triplet energy losses, has attracted extensive attention from researchers due to its simple material preparation, excellent processability, and good versatility.[33–37]

A wide range of conventional polymers, including poly(methyl methacrylate) (PMMA),[38–40] polyvinyl alcohol (PVA),[41–44] and sodium alginate (SA),[45–49] have been extensively explored as polymer matrices to construct RTP materials. Although these linear polymer-based systems achieve effective phosphorescent emission, their RTP performance remains suboptimal due to the limited confinement effect of the matrix on chromophores—a critical factor in suppressing non-radiative decay pathways.[50–54] Moreover, current research on RTP materials predominantly focuses on film or powder forms,[55,56] with scant exploration into the fabrication of high-precision complex structures, particularly three-dimensional (3D) architectures.[57–59] Consequently, there is a pressing need to develop novel polymer-based RTP systems that simultaneously enhance phosphorescence efficiency and enable high-precision fabrication of complex 3D structures, thereby bridging advanced material design and practical applications.

As an innovative rapid prototyping technology, 3D printing offers unparalleled capabilities for fabricating complex geometric

[a] *Shandong Key Laboratory of Renewable Membrane Materials, College of Materials Science and Engineering, Qingdao University, Qingdao 266071, P. R. China. E-mail: hlou@qdu.edu.cn*

[b] *Frontiers Science Center for Cell Responses, State Key Laboratory of Medicinal Chemical Biology, Key Laboratory of Bioactive Materials, Ministry of Education, and College of Life Sciences, Nankai University, Tianjin 300350, P. R. China. E-mail: dingd@nankai.edu.cn*

† Electronic supplementary information (ESI) available. See DOI: https://doi.org/10.1039/d5qm00369e

structures tailored to designers' requirements, making it particularly advantageous for constructing 3D RTP models.[60–65] For instance, Wu *et al.*[66] achieved the construction of 3D RTP models by combining direct ink writing 3D printing technology with polysaccharide-based RTP materials. Nevertheless, the current application of 3D printing for constructing RTP models predominantly relies on material extrusion techniques, which are limited by low printing precision. In contrast, photocuring 3D printing technology, renowned for its high precision, has garnered significant attention in the field of material fabrication.[67–71] This technique operates by selectively irradiating photosensitive resins with ultraviolet light, inducing layer-by-layer polymerization and cross-linking reactions that transform the liquid resin into a solid structure.[72,73] Despite its widespread adoption in material molding, the application of photocuring 3D printing in the construction of 3D models with outstanding RTP performance remains underexplored.

Herein, we present a universal strategy for fabricating high-precision 3D RTP models with ultralong lifetimes through micro-doping carbazole-based chromophores into commercially available photocurable resins, coupled with advanced photocurable 3D printing technology. The cross-linked polymer network architecture formed upon curing of the photocurable resin exhibits remarkable rigidity,[74–76] which effectively suppresses non-radiative transitions of the embedded chromophores. Furthermore, the cross-linked network serves as an efficient barrier against oxygen and moisture-induced triplet exciton quenching, thereby facilitating robust RTP emission. The selected commercial photocurable resins, primarily composed of acrylate monomers, photoinitiators, and crosslinkers, offer distinct advantages including superior rigidity, low cost, and excellent processability.[77] The chromophore series, comprising 9H-carbazole-2,7-dicarboxylic acid (Cbda), 5H-benzo[*B*]-carbazole (5Bcz), 7H-benzo[*c*]carbazole (7Bcz), 11H-benzo[*a*]-carbazole (11Bcz), 9H-dibenzo[*a*,*c*]carbazole (9Dbcz), and 7H-dibenzo[*c*,*g*]carbazole (Dbcz), are structurally characterized by carbazole cores functionalized with diverse substituents. Utilizing the doping approach, a series of photocurable RTP resins (Cbda-SR, 5Bcz-SR, 7Bcz-SR, 11Bcz-SR, 9Dbcz-SR, and Dbcz-SR) were successfully engineered by incorporating these carbazole derivatives into UV-curable standard resin (SR) at optimized ratios (Fig. 1). Following UV curing, these resins demonstrate remarkable afterglow emissions spanning cyan to red, with phosphorescence lifetimes (τ_p) extending up to 1.8 s. Through the synergistic utilization of digital light processing (DLP) 3D printing, one of the photocurable 3D printing technologies, complex 3D and 2D RTP models with ultralong lifetimes and high precision are successfully fabricated.[78–80] Notably, these photocurable RTP resins demonstrate full compatibility with commercial photocurable 3D printing systems, requiring no hardware modifications or specialized equipment. The printed RTP models exhibit superior mechanical integrity and optical transparency, making them suitable for practical applications. Capitalizing on their exceptional multicolor afterglow characteristics, these RTP models have been successfully implemented in advanced anti-counterfeiting and information encryption applications, demonstrating their potential for real-world technological applications.

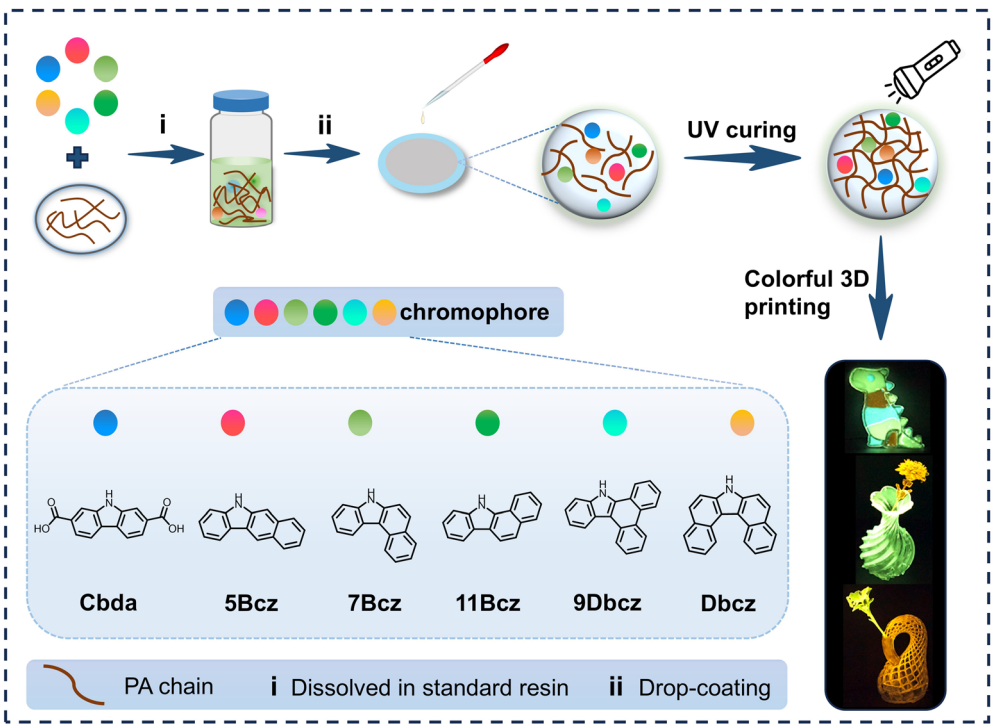

Fig. 1 Design strategy of multicolor 3D RTP models by micro-doping various carbazole-based chromophores into photocurable resins with subsequent UV curing treatment.

Results and discussion

The photophysical properties of chromophore molecules

Prior to doping into the photocurable resins, the optical properties of 9H-carbazole-2,7-dicarboxylic acid (Cbda), 5H-benzo[*B*]-carbazole (5Bcz), 7H-benzo[*c*]carbazole (7Bcz), 11H-benzo[*a*]carbazole (11Bcz), 9H-dibenzo[*a*,*c*]carbazole (9Dbcz), and 7H-dibenzo-[*c*,*g*]carbazole (Dbcz) were first investigated. The UV-visible absorption and steady-state photoluminescence (PL) spectra of these six chromophores in *N*,*N*-dimethylformamide (DMF) are shown in Fig. 2a–f. The black lines in the figures indicate that the absorption of these chromophores ranges from 305 nm to 373 nm, indicating a broad absorption range.

Upon excitation at 312 nm, these six chromophores exhibit fluorescence peaks ranging from 376 nm to 420 nm, which is consistent with their blue-purple color (Fig. 2a–f). Similarly, under 365 nm excitation, the chromophore solutions also display blue-purple fluorescence, with the fluorescence peaks shifting from 380 nm to 425 nm (Fig. S1, ESI†). The fluorescence lifetimes of the chromophore solutions were also measured under 375 nm excitation, revealing lifetimes between 4.3 ns and 16 ns (Fig. S2 and Table S1, ESI†). To investigate the differences in fluorescence between the chromophore powders and solutions, the fluorescence spectra and lifetimes of the solid powders were also characterized. As shown in Fig. S3 and S4 (ESI†), under 312 nm and 365 nm excitation, the fluorescence peaks of the solid powders (Cbda, 5Bcz, 7Bcz, 11Bcz, 9Dbcz, and Dbcz) range from 400 nm to 490 nm. Besides, the fluorescence lifetimes of these solid powders range between 2.3 ns and 9.6 ns (Fig. S5, ESI†), demonstrating typical fluorescence behavior. Notably, the fluorescence peaks of the solid powders exhibit a red shift compared to those of the solutions. This observation can be preliminarily attributed to the varying degrees of conjugation in carbazole molecules connected to different functional groups, which are influenced by their molecular states and ultimately modulate their emission characteristics.[81–87]

The photophysical properties of doped films

To exclude the effect of the SR's own luminescent properties on the doped films, the photophysical characteristics of the pure SR film after UV curing were also investigated. The normalized steady-state emission and delayed PL spectra of the pure SR film are presented in Fig. S6a and b (ESI†). Under 312 nm and 365 nm UV excitation, while the phosphorescence spectrum shows a slight redshift compared to the fluorescence spectrum, both the fluorescence and phosphorescence peaks of the pure SR film are observed at 440 nm. Notably, although the undoped SR film exhibits a strong deep blue fluorescence, no significant afterglow is observed by the naked eye after the excitation source is turned off. The intrinsic phosphorescence lifetime of the pure SR film is measured to be approximately 0.3 ms (Fig. S6c and d, ESI†).

After confirming the weak phosphorescence of the pure SR film, the photophysical properties of SR films doped with various carbazole-based chromophores were systematically investigated. Through systematic evaluation of 9Dbcz-SR with varying doping ratios (9Dbcz/SR = 1/200, 1/400, and 1/600, by weight), it was revealed that 9Dbcz-SR with a ratio of 1/400 exhibited optimal phosphorescence performance, showing a significantly higher emission intensity and longer lifetime (1837 ms) than 9Dbcz-SR with other doping ratios (Fig. S7, ESI†). When trace amounts of

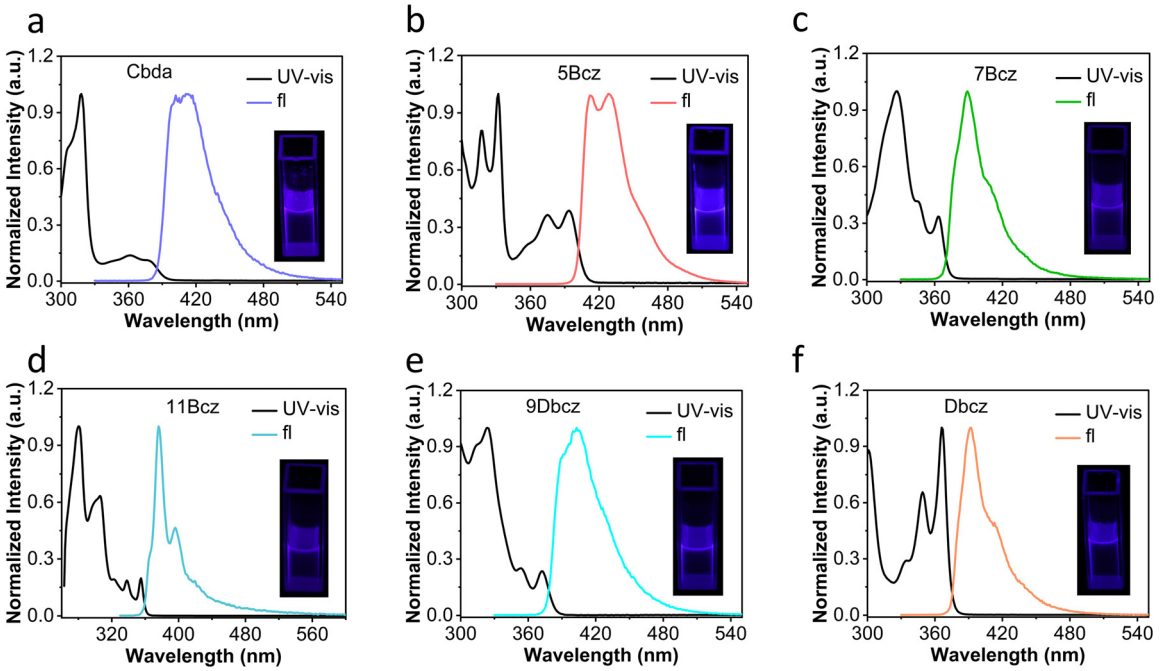

Fig. 2 The absorption (black line) and steady-state PL spectra (λ_{ex} = 312 nm) of (a) Cbda, (b) 5Bcz, (c) 7Bcz, (d) 11Bcz, (e) 9Dbcz and (f) Dbcz in DMF solution. The insets show the fluorescence photographs of the corresponding chromophore solutions.

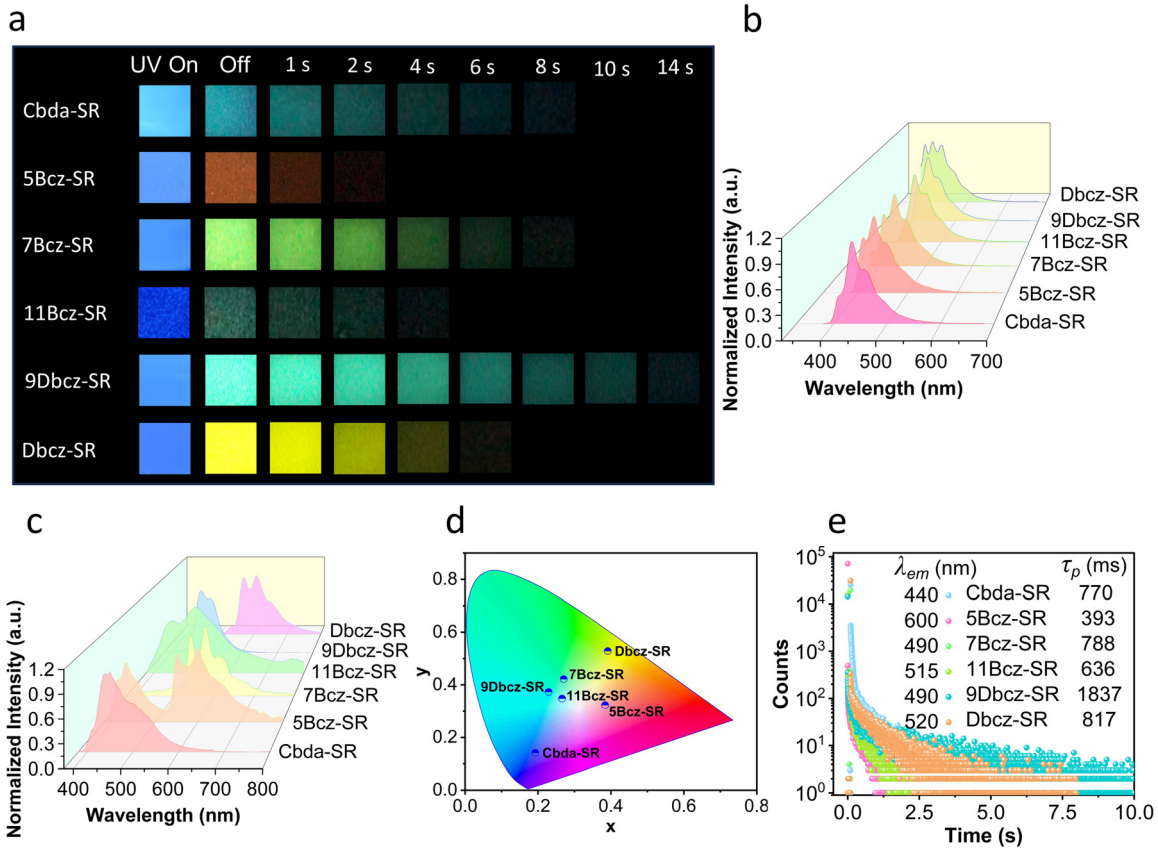

Fig. 3 (a) Luminescence photos of doped SR films upon 365 nm UV irradiation. (b) Normalized steady-state PL spectrum of doped SR films (λ_{ex} = 365 nm). (c and d) Normalized delayed PL spectrum (t_d = 1 ms) (c) under 365 nm excitation and the corresponding CIE coordinates (d) of doped SR films. (e) Time-resolved emission-decay spectra of the doped SR films under 365 nm UV excitation.

the chromophores (chromophore/SR = 1/400, mass ratio) are uniformly mixed with SR and cured under UV irradiation, the resulting Cbda-SR, 5Bcz-SR, 7Bcz-SR, 11Bcz-SR, 9Dbcz-SR, and Dbcz-SR films emit blue fluorescence under 365 nm UV excitation (Fig. 3a). Upon cessation of irradiation, all six films exhibit bright afterglow under ambient conditions, with the afterglow colors being blue, red, yellow-green, green, cyan, and yellow, respectively. Notably, the 9Dbcz-SR film displays an ultra-long cyan afterglow lasting up to approximately 14 s.

The normalized steady-state PL spectra of the six doped films under 365 nm excitation reveal fluorescence peaks between 400 nm and 440 nm, which are consistent with the fluorescence images (Fig. 3b), while the normalized delayed PL spectra of these six doped films show phosphorescence peaks ranging from 440 nm to 600 nm, often accompanied by dual-peak features (Fig. 3c). Further analysis in Fig. S8 (ESI†) demonstrates that, under 365 nm excitation, the 5Bcz-SR film exhibits a short-wavelength peak at 440 nm, which is consistent with the phosphorescence peak of the pure SR film. The Commission Internationale de l'Eclairage (CIE) coordinates of Cbda-SR, 5Bcz-SR, 7Bcz-SR, 11Bcz-SR, 9Dbcz-SR, and Dbcz-SR films are also measured as (0.19, 0.14), (0.38, 0.32), (0.27, 0.42), (0.26, 0.34), (0.22, 0.37), and (0.39, 0.52), respectively (Fig. 3d). The time-resolved emission-decay profiles under 365 nm excitation reveal that the τ_p values of these films are 770 ms, 393 ms, 788 ms, 636 ms, 1837 ms, and 817 ms, respectively (Fig. 3e and Fig. S9, ESI†). Given the dual-peak phosphorescence emission, the τ_p values of 5Bcz-SR, 7Bcz-SR, 9Dbcz-SR, and Dbcz-SR films at 560 nm, 530 nm, 520 nm, and 560 nm, respectively, are also characterized (Fig. S10, ESI†). Additionally, the luminescence quantum yields of these six polymer films under 365 nm excitation are calculated to be 56.01%, 50.27%, 59.36%, 59.66%, 67.24%, and 34.60%, respectively, demonstrating the excellent luminescence properties of these doped SR films. The results reveal that the pure SR film exhibits a low QY of only 1.24%. In contrast, the doped films show significantly enhanced quantum yields, demonstrating the effectiveness of the doping strategy (Table S2, ESI†). Furthermore, when the excitation wavelength is switched to 312 nm, these six doped SR films exhibit persistent afterglow similar to that upon 365 UV irradiation (Fig. S11–S14 and Table S3, ESI†). The ultralong organic phosphorescence (UOP) emission of these doped SR films can be attributed to the efficient ISC process within the carbazole-based chromophores and the rigid environment provided by the cross-linked polymer matrix. The rigid matrix formed after the UV-induced curing reaction of the photocurable resin, on one hand, effectively restricts the molecular motion of chromophores and minimizes vibrational energy loss. On the other hand, the cross-linked network could also suppress the quenching effect of oxygen

and water on triplet excitons, which is also beneficial to enhance the RTP emission.

The mechanical properties, thermal stability and printing process of doped SRs

Given that mechanical properties are also very important for the practical application of the RTP models, the tensile stress–strain tests were further conducted for the doped SR films. As shown in Fig. 4a, 5Bcz-SR, 7Bcz-SR, 9Dbcz-SR, and Dbcz-SR films all exhibit high stress values at low strains, ranging from 30 MPa to 42 MPa. Notably, the Dbcz-SR film achieves the highest stress value of 42 MPa at a strain of 1.4%, demonstrating exceptional mechanical strength. Differential scanning calorimetry (DSC) analysis reveals that the glass transition temperatures (T_g) of the doped films are nearly identical, approximately 70 °C, which could fulfill the requirements for use under room temperature conditions (Fig. 4b and Fig. S15, ESI†). Besides, thermogravimetric analysis (TGA) of the doped films (Cbda-SR, 5Bcz-SR, 7Bcz-SR, 11Bcz-SR, 9Dbcz-SR, and Dbcz-SR) reveals that significant mass loss began around 330 °C, further confirming their excellent thermal stability (Fig. 4c and Fig. S16, ESI†). X-ray diffraction (XRD) analysis was also performed to evaluate the inner structure of the doped SR films. The broad and structureless patterns suggest that the resin formed a uniform amorphous film after curing (Fig. 4d).

Additionally, tensile stress–strain tests and thermal stability tests were conducted for the pure SR films, which demonstrated similar mechanical strength and thermal stability (Fig. S17, ESI†). These results indicate that trace doping of chromophores has minimal impact on the mechanical properties and thermal stability of the resin. With the confirmation of excellent RTP and mechanical properties of the doped SR film, the application of the doped SR in DLP 3D printing was investigated. The printing process, as illustrated in Fig. 4e, relies on a light source (405 nm) to cure the liquid resin layer by layer using photopolymerization technology, gradually constructing a 3D object with a precise structure. Fig. 4f shows the printing

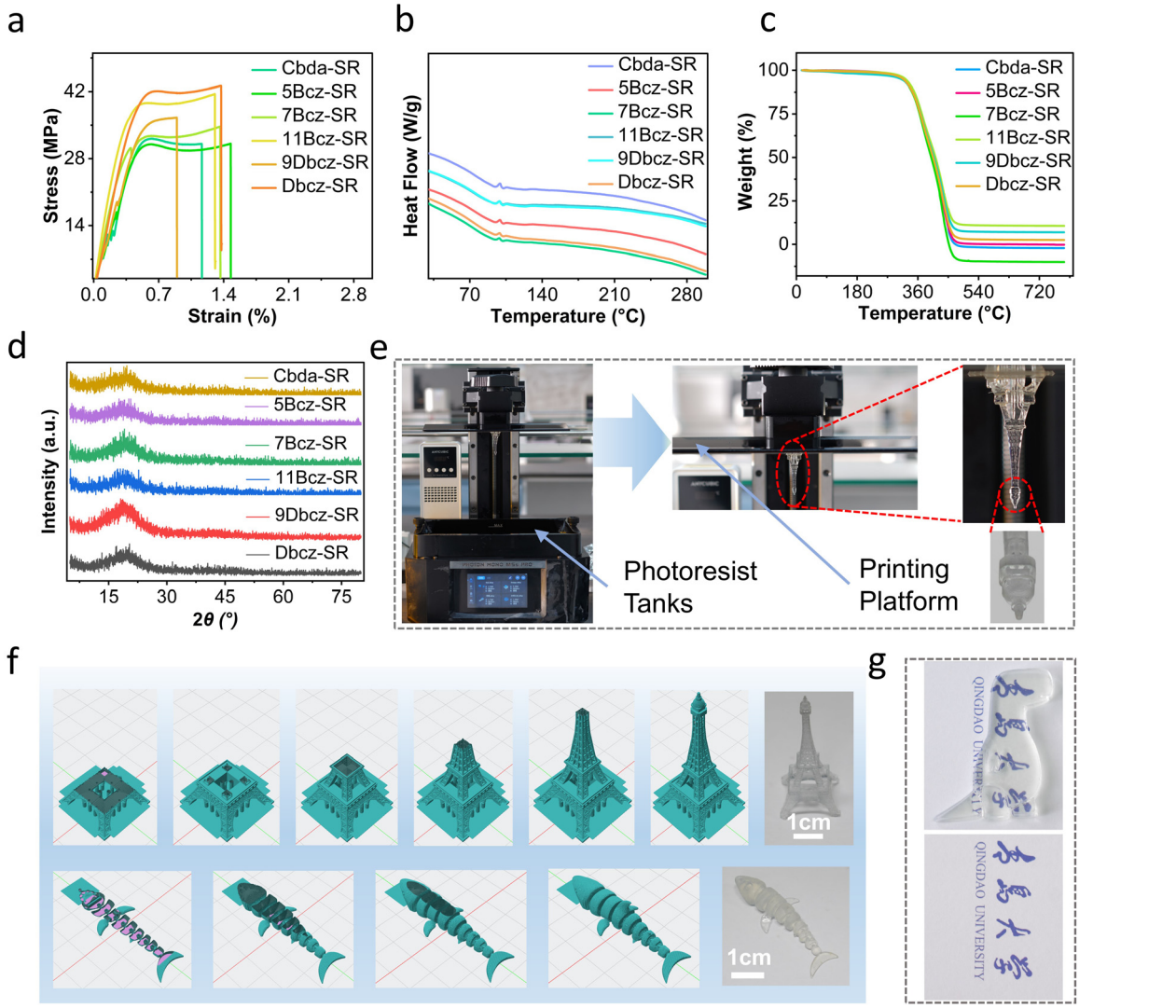

Fig. 4 (a) Tensile stress–strain curves, (b) DSC curves, (c) TGA curves, and (d) XRD patterns of different doped films. (e) Image of the DLP 3D printing process. (f) Image of the 3D modeling and slicing printing process. (g) Dinosaur 3D model with high transparency (thickness: 8 mm).

process and the final models of the Eiffel Tower and a hinged shark, both of which exhibit high precision and fine surface details. More interestingly, the hinge structure of the hinged shark provides a certain degree of flexibility. As shown in Fig. S18 (ESI†), this hinge structure for hinged sharks enables various shape transformations, breaking the limitation of traditional phosphorescent components being confined to fixed shapes. Besides, the printed 3D models exhibit outstanding transparency (Fig. 4g), highlighting their potential for broader applications in fields requiring high optical clarity.

The anti-counterfeiting and information encryption applications

To demonstrate the potential of carbazole molecule-doped SRs in 3D anti-counterfeiting and encryption applications, a series of 3D models were fabricated using DLP 3D printing. As illustrated in Fig. 5a, using a computer-aided 3D printing program and a photo-curing 3D printer, six high-precision miniatures were successfully printed, each exhibiting distinct afterglow colors. From left to right, these models correspond to the doped chromophores of Cbda, 5Bcz, 7Bcz, 11Bcz, 9Dbcz, and Dbcz. Under 365 nm ultraviolet excitation, all six models display identical blue fluorescence. However, upon removal of the excitation source, they exhibit unique afterglow colors, enabling effective 3D anti-counterfeiting.

To further explore this capability, numerous 3D models with varying afterglow colors (Fig. S19 and Video S1, ESI†) were further prepared for applications in anti-counterfeiting. Fig. 5b highlights the intricate details of a hollow vase, a Chinese

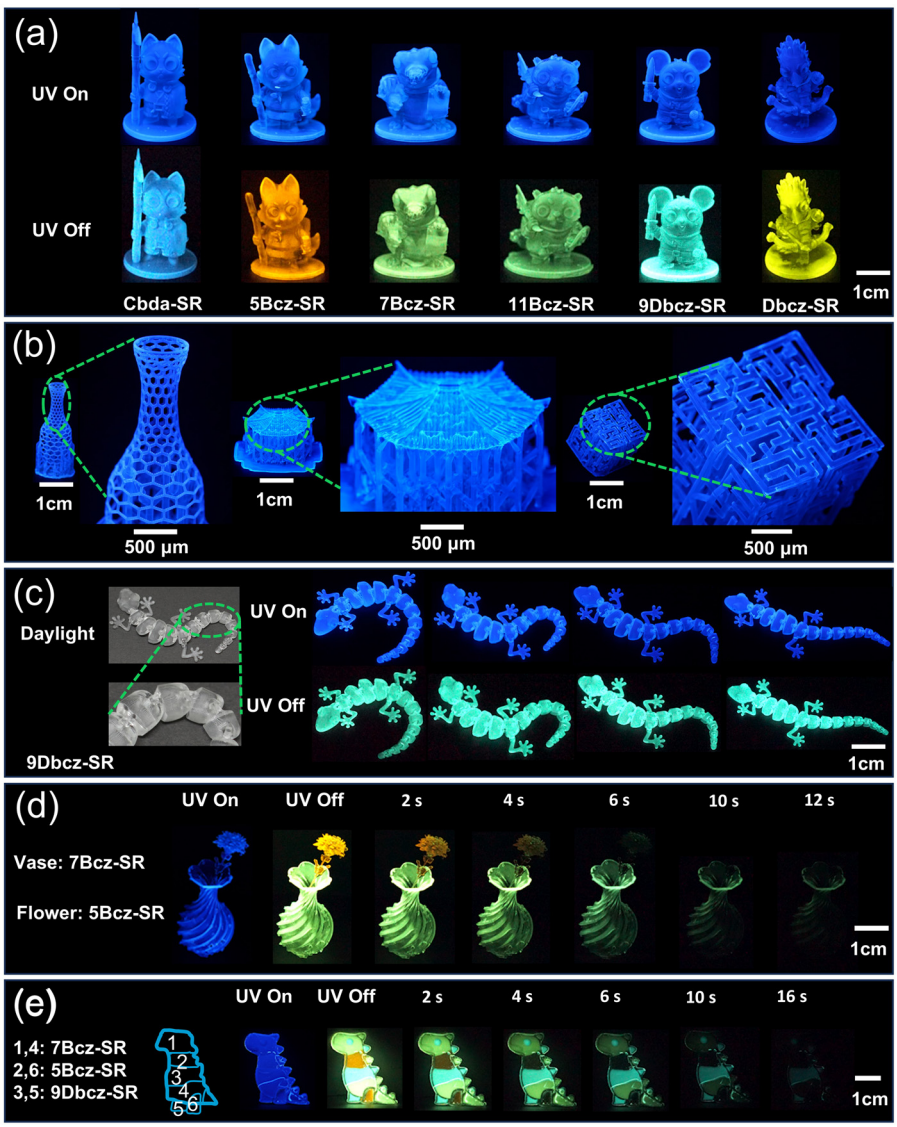

Fig. 5 Demonstration of the anti-counterfeiting application of multi-color afterglow 3D models fabricated by DLP 3D printing. (a) 3D miniature models doped with different carbazole chromophores. (b) Enlarged view of the details of the hollow vase, Chinese pavilion and three-dimensional maze. (c) Different movement trajectories of the same hinged lizard upon UV irradiation and enlarged view of the hinge structure details under daylight. (d) 3D anti-counterfeiting model assembled with orange-red flowers (5Bcz-SR) and green vase (7Bcz-SR). (e) Colorful afterglow dinosaur 3D model with different chromophores added to different parts (all models were photographed under 365 nm excitation).

pavilion, and a maze, showcasing the high precision of the printed models and their potential for real-life applications. While immovable 3D RTP models can be printed, some movable 3D RTP models were also printed utilizing DLP 3D printing technology.

As shown in Fig. 5c, a 3D lizard RTP model featuring a hinge structure (enlarged view) was printed using 9Dbcz-SR as the photocurable resin. Owing to the hinge structure, the same model could be presented in different shapes (Video S2, ESI†). Thus, the different movement trajectories of the same hinged lizard can be clearly visualized along with the fine RTP properties, further increasing the anti-counterfeiting level of the models. Furthermore, the 3D printed structures are suitable for creating assembled products with diverse afterglow colors. As shown in Fig. 5d, under UV excitation, both the flowers and the vase emit bright blue fluorescence. Upon turning off the UV light, the vase exhibits a green afterglow lasting up to 12 s, while the orange-red flowers fade in less than 6 s (Video S3, ESI†). Fig. S20 (ESI†) presents additional combinations of vases and flowers, leveraging differences in afterglow colors and durations to achieve multi-dimensional anti-counterfeiting effects. In Fig. 5e, a dinosaur model with spatially resolved afterglow emissions is designed by incorporating different chromophores into distinct regions. The red section corresponds to 5Bcz-SR, the green section to 7Bcz-SR, and the cyan afterglow to 9Dbcz-SR, which persists for approximately 16 s, demonstrating the longest afterglow duration (Video S4, ESI†). This approach highlights the versatility of the material in creating complex, multi-colored afterglow patterns for advanced anti-counterfeiting applications.

To broaden the applications of RTP models with varying degrees of dimensionality in anti-counterfeiting, a series of 2D RTP models with high precision were also fabricated. As shown in Fig. 6a, the 2D models doped with 5Bcz, 7Bcz, 11Bcz, 9Dbcz, and Dbcz demonstrate orange-red, yellow-green, green, cyan, and yellow afterglow, respectively, which is consistent with the 3D RTP models. These results clearly demonstrate that both 2D and 3D models can achieve high precision and effective anti-

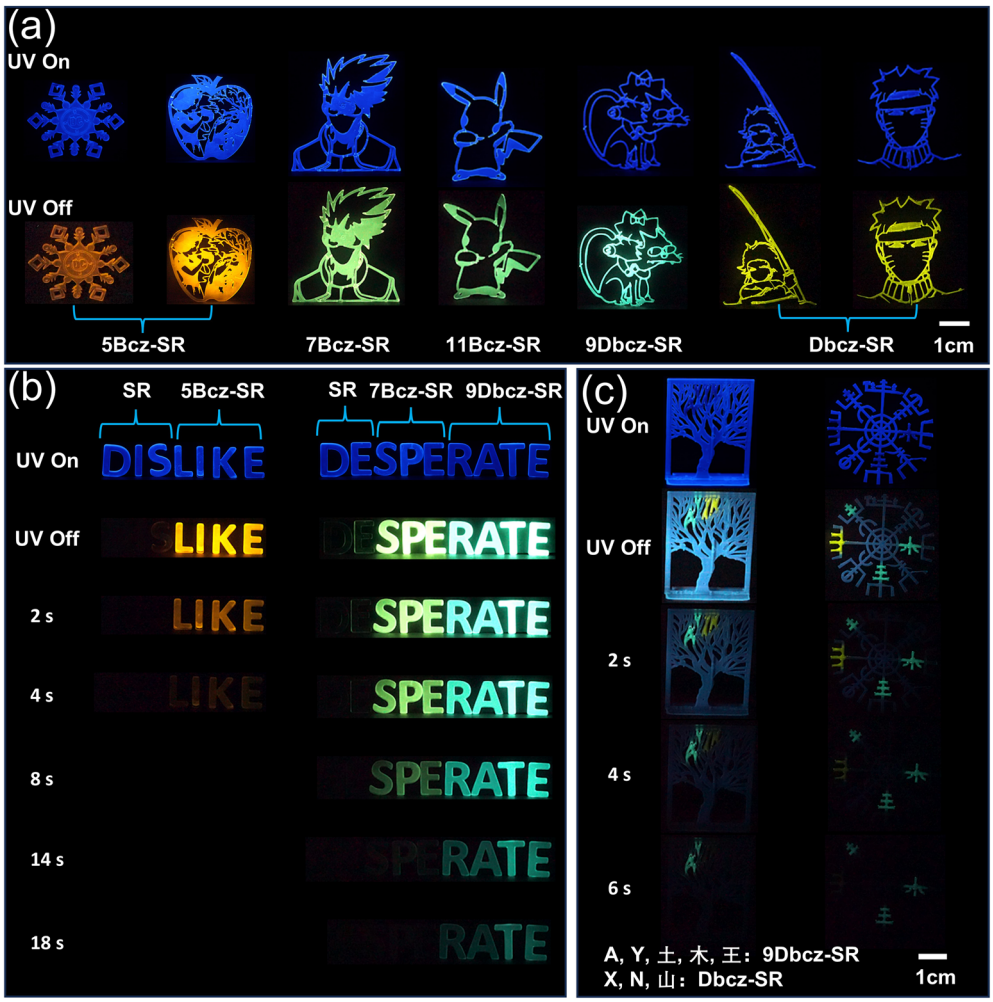

Fig. 6 Demonstration of the application of multi-color afterglow 2D models in anti-counterfeiting and multiple information encryption under ambient conditions. (a) The anti-counterfeiting application of 2D models with different shapes and afterglow colors. (b) Letter encryption models prepared with different afterglow times. (c) The blue tree 3D model and the compass model for multi-color afterglow information encryption (all models were photographed under 365 nm excitation).

counterfeiting by utilizing chromophore-doped SRs. More intriguingly, taking advantage of the distinct afterglow colors and durations of different carbazole molecule-doped SRs, a letter encryption model (Fig. 6b and Video S5, ESI†) and an afterglow encryption model (Fig. 6c) were constructed. Under 365 nm UV excitation, the letters ''DISLIKE'' and ''DESPERATE'' emit blue fluorescence. Upon turning off the UV light, the letters ''LIKE'' with an orange-red afterglow and the letters ''SPE'' and ''RATE'' with green and cyan afterglow colors became visible within approximately 2 s. After about 14 s, only the cyan letters ''RATE'' remain, demonstrating a multi-layered encryption effect.

In Fig. 6c, the tree and compass models exhibit uniform bright blue emission under UV excitation. After removing the excitation source, hidden information is revealed on the tree branches, including cyan letters ''A'' and ''Y'' and yellow letters ''X'' and ''N'', while the compass model displays a yellow Chinese character ''山'' and cyan characters ''土'', ''木'', as well as ''王'' arranged clockwise, representing the first layer of encrypted information. As time progresses, the yellow character ''山'' gradually fades after approximately 4 s, leaving only the cyan characters ''土'', ''木'', and ''王'' visible after 6 s, which constitute the second layer of encrypted information (Video S6, ESI†). These models consistently maintain high-fidelity shapes and exhibit a wide range of afterglow colors, including orange, yellow, green, cyan, and blue, underscoring their practical value in multidimensional anti-counterfeiting and encryption applications. To verify the barrier properties of the cured SRs to oxygen and water, the afterglow performance of the 3D RTP models under vacuum and water immersion conditions was further investigated. As illustrated in Fig. S21 (ESI†), the 3D RTP models exhibit remarkable water resistance, with their afterglow color and duration in aqueous solutions consistent with those under dry conditions.

Additionally, the afterglow duration of the 3D RTP models remains unchanged in atmospheric environments compared to that under vacuum conditions (Fig. S22, ESI†), further confirming the ability of the cured SRs to effectively shield against oxygen-induced quenching. Remarkably, long-term environmental stability evaluation reveals that the 3D afterglow models still preserve superior long afterglow performance over a 4-month period (Fig. S23, ESI†). These superior characteristics significantly enhance the application potential of 3D afterglow devices in multilevel encryption and anti-counterfeiting, enabling them to maintain stable RTP performance even in challenging environments such as water or hyperoxic environments.

Conclusions

In summary, we have developed a general strategy to construct 3D RTP models with precise structures and ultralong lifetimes by micro-doping carbazole-based chromophores into photocurable resins and combining them with photocurable 3D printing technology. The highly cross-linked and rigid microenvironment formed after the curing of SR effectively suppresses the molecular motion-induced vibrational energy loss and minimizes the quenching effect of oxygen and water on triplet excitons. As a result, the cured carbazole-doped SR exhibits an exceptionally long phosphorescence lifetime of up to 1.8 s. By adjusting the differences in the dopant molecular structure, multicolor afterglow from cyan to red are successfully realized. Afterwards, utilizing DLP 3D printing technology, a series of multicolor 3D and 2D RTP models with precise structures and ultralong lifetimes are constructed based on carbazole-doped SR. Besides, the RTP models exhibit excellent mechanical properties and thermal stability, and their afterglow time in aqueous solutions and air environments is nearly the same as that under dry and oxygen-free conditions, respectively. Given the good tunability of 3D printing blueprints and the excellent RTP properties of the printed models, these multidimensional models are successfully employed in advanced anti-counterfeiting and encryption applications. Notably, more diverse and movable RTP models have also been successfully constructed through the combination of printed models and the introduction of hinge structures, respectively. We believe this work represents an important step forward in the development of 3D afterglow devices and expands the potential applications of RTP materials in the field of 3D printing.

Author contributions

R. D. prepared the manuscript under the supervision of H. O. and D. D. All authors contributed to the general discussion.

Conflicts of interest

There are no conflicts to declare.

Data availability

The authors confirm that the data supporting the findings of this study are available within the article and/or its ESI.†

Acknowledgements

This work was supported by the National Natural Science Foundation of China (U22A20250, U22A20131, U21A2097, 52072193 and 52361165657), the Shandong Provincial Natural Science Foundation (ZR2024QE030 and ZR2023YQ040), the Support Plan on Science and Technology for Youth Innovation of Universities in Shandong Province (2023KJ230), and the Young Talent of Lifting Engineering for Science and Technology in Shandong, China (SDAST2024QTA069).

References

1 J. Jin, H. Jiang, Q. Yang, L. Tang, Y. Tao, Y. Li, R. Chen, C. Zheng, Q. Fan, K. Y. Zhang, Q. Zhao and W. Huang, Thermally activated triplet exciton release for highly efficient tri-mode organic afterglow, *Nat. Commun.*, 2020, **11**, 842.
2 Y. Tao, Q. Wang, C. Yang, Q. Wang, Z. Zhang, T. Zou, J. Qin and D. Ma, A Simple Carbazole/Oxadiazole Hybrid Molecule: An Excellent Bipolar Host for Green and Red

Phosphorescent OLEDs, *Angew. Chem., Int. Ed.*, 2008, **47**, 8104–8107.
3 Z.-Y. Zhang, W.-W. Xu, W.-S. Xu, J. Niu, X.-H. Sun and Y. Liu, A Synergistic Enhancement Strategy for Realizing Ultralong and Efficient Room-Temperature Phosphorescence, *Angew. Chem., Int. Ed.*, 2020, **59**, 18748–18754.
4 L. Xu, K. Zhou, H. Ma, A. Lv, D. Pei, G. Li, Y. Zhang, Z. An, A. Li and G. He, Ultralong Organic Phosphorescent Nanocrystals with Long-Lived Triplet Excited States for Afterglow Imaging and Photodynamic Therapy, *ACS Appl. Mater. Interfaces*, 2020, **12**, 18385–18394.
5 Y. Zhang, J. Miao, J. Xiong, K. Li and C. Yang, Rigid Bridge-Confined Double-Decker Platinum(II) Complexes Towards High-Performance Red and Near-Infrared Electroluminescence, *Angew. Chem., Int. Ed.*, 2022, **61**, e202113718.
6 Z. Wang, H. Yuan, Y. Zhang, D. Wang, J. Ju and Y. Tan, Recent progress in organic color-tunable phosphorescent materials, *J. Mater. Sci. Technol.*, 2022, **101**, 264–284.
7 B. Song, W. Shao, J. Jung, S.-J. Yoon and J. Kim, Organic Light-Emitting Diode Employing Metal-Free Organic Phosphor, *ACS Appl. Mater. Interfaces*, 2020, **12**, 6137–6143.
8 Y. Fan, Q. Li and Z. Li, Afterglow bio-applications by utilizing triplet excited states of organic materials, *Sci. China: Chem.*, 2023, **66**, 2930–2940.
9 D. Ding and B. Z. Tang, Advances in Improving Healthcare with Aggregation-Induced Emission, *Adv. Healthcare Mater.*, 2021, **10**, 2102499.
10 H. Zhang and B. Z. Tang, Through-Space Interactions in Clusteroluminescence, *JACS Au*, 2021, **1**, 1805–1814.
11 X. Yang and D. Yan, Long-afterglow metal–organic frameworks: reversible guest-induced phosphorescence tunability, *Chem. Sci.*, 2016, **7**, 4519–4526.
12 Z. Li, Y. Han, F. Nie, M. Liu, H. Zhong and F. Wang, Bright and Robust Phosphorescence Achieved by Non-Covalent Clipping, *Angew. Chem., Int. Ed.*, 2021, **60**, 8212–8219.
13 D. Li, Y. Yang, J. Yang, M. Fang, B. Z. Tang and Z. Li, Completely aqueous processable stimulus responsive organic room temperature phosphorescence materials with tunable afterglow color, *Nat. Commun.*, 2022, **13**, 347.
14 M. S. Kwon, Y. Yu, C. Coburn, A. W. Phillips, K. Chung, A. Shanker, J. Jung, G. Kim, K. Pipe, S. R. Forrest, J. H. Youk, J. Gierschner and J. Kim, Suppressing molecular motions for enhanced room-temperature phosphorescence of metal-free organic materials, *Nat. Commun.*, 2015, **6**, 8947.
15 Q. Wang, X. Dou, X. Chen, Z. Zhao, S. Wang, Y. Wang, K. Sui, Y. Tan, Y. Gong, Y. Zhang and W. Z. Yuan, Reevaluating Protein Photoluminescence: Remarkable Visible Luminescence upon Concentration and Insight into the Emission Mechanism, *Angew. Chem., Int. Ed.*, 2019, **58**, 12667–12673.
16 H. Qiu, W. Wang, H. Cheng, Y. Lu, M. Li, H. Chen, X. Fang, C. Jiang and Y. Zheng, Triple optically modulated and enzymatically responsive organic afterglow materials for dynamic anti-counterfeiting, *Mater. Chem. Front.*, 2022, **6**, 1824–1834.
17 Z.-Y. Zhang, Y. Chen and Y. Liu, Efficient Room-Temperature Phosphorescence of a Solid-State Supramolecule Enhanced by Cucurbit[6]uril, *Angew. Chem., Int. Ed.*, 2019, **58**, 6028–6032.
18 J. Song, Y. Zhou, Z. Pan, Y. Hu, Z. He, H. Tian and X. Ma, An elastic organic crystal with multilevel stimuli-responsive room temperature phosphorescence, *Matter*, 2023, **6**, 2005–2018.
19 B. Ding, L. Ma, Z. Huang, X. Ma and H. Tian, Engendering persistent organic room temperature phosphorescence by trace ingredient incorporation, *Sci. Adv.*, 2021, **7**, eabf9668.
20 A. Abe, K. Goushi, M. Mamada and C. Adachi, Organic Binary and Ternary Cocrystal Engineering Based on Halogen Bonding Aimed at Room-Temperature Phosphorescence, *Adv. Mater.*, 2024, **36**, 2211160.
21 O. Bolton, K. Lee, H.-J. Kim, K. Y. Lin and J. Kim, Activating efficient phosphorescence from purely organic materials by crystal design, *Nat. Chem.*, 2011, **3**, 205–210.
22 Z. Yin, Z. Xie, X. Zhang, Y. Xue, D. Zhang and B. Liu, Cocrystallization-Induced Red Ultralong Organic Phosphorescence, *Angew. Chem., Int. Ed.*, 2025, **64**, e202417868.
23 X. Zhao, X. Zhou, Q. Cheng and Y. Liu, Blue phosphorescent solid supramolecular assemblies between hydroxypropyl-β-cyclodextrin and triazine derivatives for achieving multicolor delayed fluorescence, *Nano Today*, 2025, **60**, 102561.
24 T. Zhang, X. Ma, H. Wu, L. Zhu, Y. Zhao and H. Tian, Molecular Engineering for Metal-Free Amorphous Materials with Room-Temperature Phosphorescence, *Angew. Chem., Int. Ed.*, 2020, **59**, 11206–11216.
25 F. Xiao, H. Gao, Y. Lei, W. Dai, M. Liu, X. Zheng, Z. Cai, X. Huang, H. Wu and D. Ding, Guest-host doped strategy for constructing ultralong-lifetime near-infrared organic phosphorescence materials for bioimaging, *Nat. Commun.*, 2022, **13**, 186.
26 X.-Y. Liu, W. P. Lustig and J. Li, Functionalizing Luminescent Metal–Organic Frameworks for Enhanced Photoluminescence, *ACS Energy Lett.*, 2020, **5**, 2671–2680.
27 M. Gao, J. Ren, Y. Gong, M. Fang, J. Yang and Z. Li, A new insight into aggregation structure of organic solids and its relationship to room-temperature phosphorescence effect, *Aggregate*, 2024, **5**, e462.
28 B. Ding, X. Ma and H. Tian, Recent Advances of Pure Organic Room Temperature Phosphorescence Based on Functional Polymers, *Acc. Mater. Res.*, 2023, **4**, 827–838.
29 X. Ma, C. Xu, J. Wang and H. Tian, Inside Cover: Amorphous Pure Organic Polymers for Heavy-Atom-Free Efficient Room-Temperature Phosphorescence Emission, *Angew. Chem., Int. Ed.*, 2018, **57**, 10774.
30 N. Gan, X. Zou, Z. Qian, A. Lv, L. Wang, H. Ma, H.-J. Qian, L. Gu, Z. An and W. Huang, Stretchable phosphorescent polymers by multiphase engineering, *Nat. Commun.*, 2024, **15**, 4113.
31 J. Guo, C. Yang and Y. Zhao, Long-Lived Organic Room-Temperature Phosphorescence from Amorphous Polymer Systems, *Acc. Chem. Res.*, 2022, **55**, 1160–1170.
32 Z. Wang, A. Li, Z. Zhao, T. Zhu, Q. Zhang, Y. Zhang, Y. Tan and W. Z. Yuan, Accessing Excitation- and Time-Responsive Afterglows from Aqueous Processable Amorphous Polymer Films through Doping and Energy Transfer, *Adv. Mater.*, 2022, **34**, 2202182.

33 D. Li, J. Yang, M. Fang, B. Z. Tang and Z. Li, Stimulus-responsive room temperature phosphorescence materials with full-color tunability from pure organic amorphous polymers, *Sci. Adv.*, 2022, **8**, eabl8392.
34 Z.-H. Wang, C.-H. Liu, P.-Y. Fu, H.-L. Sun, L. Zheng and M. Pan, Circular Modulation Pathway of the Afterglow Color in Metal-Organic Coordination Polymer, *Adv. Opt. Mater.*, 2024, **12**, 2400424.
35 Kenry, C. Chen and B. Liu, Enhancing the performance of pure organic room-temperature phosphorescent luminophores, *Nat. Commun.*, 2019, **10**, 2111.
36 W. Zhao, Z. He and B. Z. Tang, Room-temperature phosphorescence from organic aggregates, *Nat. Rev. Mater.*, 2020, **5**, 869–885.
37 S. Xu, R. Chen, C. Zheng and W. Huang, Excited State Modulation for Organic Afterglow: Materials and Applications, *Adv. Mater.*, 2016, **28**, 9920–9940.
38 D. Lee, O. Bolton, B. C. Kim, J. H. Youk, S. Takayama and J. Kim, Room Temperature Phosphorescence of Metal-Free Organic Materials in Amorphous Polymer Matrices, *J. Am. Chem. Soc.*, 2013, **135**, 6325–6329.
39 X. Zhang, C. Qian, Z. Ma, X. Fu, Z. Li, H. Jin, M. Chen, H. Jiang and Z. Ma, A Class of Organic Units Featuring Matrix-Controlled Color-Tunable Ultralong Organic Room Temperature Phosphorescence, *Adv. Sci.*, 2023, **10**, 2206482.
40 X. Piao, T. Wang, X. Chen, G. Wang, X. Zhai and K. Zhang, Room-temperature phosphorescent transparent wood, *Nat. Commun.*, 2025, **16**, 868.
41 R. Liu, T. Jiang, D. Liu and X. Ma, A facile and green strategy to obtain organic room-temperature phosphorescence from natural lignin, *Sci. China: Chem.*, 2022, **65**, 1100–1104.
42 S. Sun, L. Ma, J. Wang, X. Ma and H. Tian, Red-light excited efficient metal-free near-infrared room-temperature phosphorescent films, *Natl. Sci. Rev.*, 2022, **9**, nwab085.
43 D. Wang, J. Gong, Y. Xiong, H. Wu, Z. Zhao, D. Wang and B. Z. Tang, Achieving Color-Tunable and Time-Dependent Organic Long Persistent Luminescence via Phosphorescence Energy Transfer for Advanced Anti-Counterfeiting, *Adv. Funct. Mater.*, 2023, **33**, 2208895.
44 Y. Zhang, L. Gao, X. Zheng, Z. Wang, C. Yang, H. Tang, L. Qu, Y. Li and Y. Zhao, Ultraviolet irradiation-responsive dynamic ultralong organic phosphorescence in polymeric systems, *Nat. Commun.*, 2021, **12**, 2297.
45 R. Wang, D. Ma, X. Kong, F. Peng, X. Cao, Y. Zhao, C. Lu and W. Shi, Metastable Supramolecular Assembly of Simple Monomers Enabled by Confinement: Towards Aqueous Phase Room Temperature Phosphorescence, *Angew. Chem., Int. Ed.*, 2024, **63**, e202409162.
46 S. Sun, Y. Zhu, T. Li, G. Wang, F. Yin, F. Li, F. Tao, L. Wang and G. Li, Ultralong sodium alginate-based room temperature phosphorescence materials with advantages of color tunability, flexibility and facile large-area fabrication, *Chem. Eng. J.*, 2024, **485**, 149751.
47 T. Wang, Z. Wang, Z. Li, Z. Chen, H. Sun, H. Yuan, H. Ou, X. Huang and Y. Tan, Accessing color-tunable afterglows from single conventional chromophore-based polysaccharide films through palette strategy, *Chem. Eng. J.*, 2024, **495**, 153026.
48 X. Dou, T. Zhu, Z. Wang, W. Sun, Y. Lai, K. Sui, Y. Tan, Y. Zhang and W. Z. Yuan, Color-Tunable, Excitation-Dependent, and Time-Dependent Afterglows from Pure Organic Amorphous Polymers, *Adv. Mater.*, 2020, **32**, 2004768.
49 C. Ren, Z. Wang, H. Ou, T. Wang, Z. Zhao, Y. Wei, H. Yuan, Y. Tan and W. Z. Yuan, Multi-Responsive Afterglows from Aqueous Processable Amorphous Polysaccharide Films, *Small Methods*, 2024, **8**, 2300243.
50 X. Zhang, Y. Cheng, J. You, J. Zhang, C. Yin and J. Zhang, Ultralong phosphorescence cellulose with excellent antibacterial, water-resistant and ease-to-process performance, *Nat. Commun.*, 2022, **13**, 1117.
51 H. Gao and X. Ma, Recent progress on pure organic room temperature phosphorescent polymers, *Aggregate*, 2021, **2**, e38.
52 W.-W. Xu, Y. Chen, Y.-L. Lu, Y.-X. Qin, H. Zhang, X. Xu and Y. Liu, Tunable Second-Level Room-Temperature Phosphorescence of Solid Supramolecules between Acrylamide–Phenylpyridium Copolymers and Cucurbit[7]uril, *Angew. Chem., Int. Ed.*, 2022, **61**, e202115265.
53 H. Sun, X. Wei, Y. He, Y. Xiao, Y. Wu, Z. Xie and T. Yu, Regulation of various photo-active UOPs in a polymer matrix by tuning intermolecular charge transfer, *Mater. Chem. Front.*, 2023, **7**, 3156–3163.
54 Y. Gao, Z. Deng, F. Wang and P. Sun, Achieving long lifetime of room-temperature phosphorescence via constructing vitrimer networks, *Mater. Chem. Front.*, 2022, **6**, 1068–1078.
55 X. Yao, H. Ma, X. Wang, H. Wang, Q. Wang, X. Zou, Z. Song, W. Jia, Y. Li, Y. Mao, M. Singh, W. Ye, J. Liang, Y. Zhang, Z. Liu, Y. He, J. Li, Z. Zhou, Z. Zhao, Y. Zhang, G. Niu, C. Yin, S. Zhang, H. Shi, W. Huang and Z. An, Ultralong organic phosphorescence from isolated molecules with repulsive interactions for multifunctional applications, *Nat. Commun.*, 2022, **13**, 4890.
56 W. Gao, Y. Su, Z. Wang, Y. Zhang, D. Zhang, P. Jia, C. Yang, Y. Li, R. Ganguly and Y. Zhao, Effect of Carbazolyl Groups on Photophysical Properties of Cyanuric Chloride, *ACS Appl. Mater. Interfaces*, 2019, **11**, 47162–47169.
57 Y. Zhang, F. Zhang, Z. Yan, Q. Ma, X. Li, Y. Huang and J. A. Rogers, Printing, folding and assembly methods for forming 3D mesostructures in advanced materials, *Nat. Rev. Mater.*, 2017, **2**, 17019.
58 D. Kong, Y. Li, B. Yang, Y. Pang, H. Yuan, C. Du and Y. Tan, 3D-Printed Hydrogels with High-Strength and Anisotropy Mediated by Chain Rigidity, *Small*, 2024, **20**, 2403052.
59 C. Zhu, J. Jin, Z. Wang, Z. Xu, M. C. Folgueras, Y. Jiang, C. B. Uzundal, H. K. D. Le, F. Wang, X. Zheng and P. Yang, Supramolecular assembly of blue and green halide perovskites with near-unity photoluminescence, *Science*, 2024, **383**, 86–93.
60 M. Zhang, Q. Guo, Z. Li, Y. Zhou, S. Zhao, Z. Tong, Y. Wang, G. Li, S. Jin, M. Zhu, T. Zhuang and S.-H. Yu, Processable circularly polarized luminescence material enables flexible stereoscopic 3D imaging, *Sci. Adv.*, 2023, **9**, eadi9944.

61 D. Kokkinis, M. Schaffner and A. R. Studart, Multimaterial magnetically assisted 3D printing of composite materials, *Nat. Commun.*, 2015, **6**, 8643.
62 J. Li and M. Pumera, 3D printing of functional microrobots, *Chem. Soc. Rev.*, 2021, **50**, 2794–2838.
63 C. Darkes-Burkey and R. F. Shepherd, High-resolution 3D printing in seconds, *Nature*, 2020, **588**, 594–595.
64 P. Somers, A. Münchinger, S. Maruo, C. Moser, X. Xu and M. Wegener, The physics of 3D printing with light, *Nat. Rev. Phys.*, 2024, **6**, 99–113.
65 Y. Xu, M. Fang, Z. Li, Y. Xue, K. Wang, F. Lin and N. Zhang, Embracing the future: The application of regenerative biomaterials in the spinal disorders, *Biomed. Technol.*, 2025, **9**, 100068.
66 P. Wu, P. Li, M. Chen, J. Rao, G. Chen, J. Bian, B. Lü and F. Peng, 3D Printed Room Temperature Phosphorescence Materials Enabled by Edible Natural Konjac Glucomannan, *Adv. Mater.*, 2024, **36**, 2402666.
67 D. Ahn, L. M. Stevens, K. Zhou and Z. A. Page, Rapid High-Resolution Visible Light 3D Printing, *ACS Cent. Sci.*, 2020, **6**, 1555–1563.
68 X. Kang, X. Li, Y. Li, X. Zhang and Y. Duan, Continuous 3D printing by controlling the curing degree of hybrid UV curing resin polymer, *Polymer*, 2021, **237**, 124284.
69 A. Vartanian, Pinpoint 3D printing, *Nat. Rev. Mater.*, 2022, **7**, 336.
70 C. Zhu, H. B. Gemeda, E. B. Duoss and C. M. Spadaccini, Toward Multiscale, Multimaterial 3D Printing, *Adv. Mater.*, 2024, **36**, 2314204.
71 J. Li, D. Liang, X. Chen, W. Sun and X. Shen, Applications of 3D printing in tumor treatment, *Biomed. Technol.*, 2024, **5**, 1–13.
72 W. Huang, Z. Zu, Y. Huang, H. Xiang and X. Liu, UV-curing 3D printing of high-performance, recyclable, biobased photosensitive resin enabled by dual-crosslinking networks, *Addit. Manuf.*, 2024, **91**, 104352.
73 D. A. Walker, J. L. Hedrick and C. A. Mirkin, Rapid, large-volume, thermally controlled 3D printing using a mobile liquid interface, *Science*, 2019, **366**, 360–364.
74 T. Xiao, L. Geng, Y. Dai, J. Zhao and C. Liu, UV-cured polymer aided phase change thermal energy storage: Preparation, mechanism and prospects, *J. Energy Storage*, 2023, **64**, 107066.
75 H. Sun, S. Shen and L. Zhu, Photo-stimuli-responsive Organic Room-Temperature Phosphorescent Materials, *ACS Mater. Lett.*, 2022, **4**, 1599–1615.
76 S. Jiang, D. Guo, F. Lin, J. Chen, Y. Miao, H. Huang, J.-W. Yang, W. Qin and Z. Chi, Time-Dependent Multicolor Afterglow from Dual Persistent Luminescence of Fluorescence and Phosphorescence in a UV-Cured Polyurethane Matrix, *ACS Mater. Lett.*, 2024, **6**, 1371–1379.
77 I. Cazin, K. Plevová, W. Alabiso, E. Vidović and S. Schlögl, Dual-Wavelength Vat Photopolymerization 3D Printing with Hybrid Acrylate-Epoxy Resins: Influence of Resin Composition on Microstructure and Mechanical Properties, *Adv. Eng. Mater.*, 2024, **26**, 2301699.
78 G. Zhu, Y. Hou, J. Xu and N. Zhao, Reprintable Polymers for Digital Light Processing 3D Printing, *Adv. Funct. Mater.*, 2021, **31**, 2007173.
79 W. Li, M. Wang, L. S. Mille, J. A. Robledo Lara, V. Huerta, T. Uribe Velázquez, F. Cheng, H. Li, J. Gong, T. Ching, C. A. Murphy, A. Lesha, S. Hassan, T. B. F. Woodfield, K. S. Lim and Y. S. Zhang, A Smartphone-Enabled Portable Digital Light Processing 3D Printer, *Adv. Mater.*, 2021, **33**, 2102153.
80 X. Peng, L. Yue, S. Liang, S. Montgomery, C. Lu, C.-M. Cheng, R. Beyah, R. R. Zhao and H. J. Qi, Multi-Color 3D Printing via Single-Vat Grayscale Digital Light Processing, *Adv. Funct. Mater.*, 2022, **32**, 2112329.
81 X. Fu, X. Zhang, C. Qian, Z. Ma, Z. Li, H. Jiang and Z. Ma, A Readily Obtained Alternative to 1H-Benzo[f]indole toward Room-Temperature Ultralong Organic Phosphorescence, *Chem. Mater.*, 2023, **35**, 347–357.
82 C. Qian, X. Zhang, Z. Ma, X. Fu, Z. Li, H. Jin, M. Chen, H. Jiang and Z. Ma, Matrix-Mediated Color-Tunable Ultralong Organic Room Temperature Phosphorescence of 7H-Benzo[c]carbazole Derivatives, *CCS Chem.*, 2023, **6**, 798–811.
83 S. Feng and Q. Zheng, Mechanism of 7H-Dibenzo[c,g]carbazole metabolism in cytochrome P450 1A1: Insights from computational studies, *J. Hazard. Mater.*, 2024, **476**, 134933.
84 Y. Zhang, Y. Su, H. Wu, Z. Wang, C. Wang, Y. Zheng, X. Zheng, L. Gao, Q. Zhou, Y. Yang, X. Chen, C. Yang and Y. Zhao, Large-Area, Flexible, Transparent, and Long-Lived Polymer-Based Phosphorescence Films, *J. Am. Chem. Soc.*, 2021, **143**, 13675–13685.
85 Y. Yang, Q. Li and Z. Li, Advances in organic room-temperature phosphorescence: design strategies, photophysical mechanisms, and emerging applications, *Mater. Chem. Front.*, 2025, **9**, 744–753.
86 S. Oner and M. R. Bryce, A review of fused-ring carbazole derivatives as emitter and/or host materials in organic light emitting diode (OLED) applications, *Mater. Chem. Front.*, 2023, **7**, 4304–4338.
87 W. Cai, L. Zuo, S. Feng, P. Hu, H. Wei, Z. Zhang, H. Wu, L. Wang, Y. Wang, G. Shi and B. Xu, Controlling the efficient and ultralong room-temperature phosphorescence of 9H-dibenzo[a,c]carbazole derivatives for erasable light printing, *Mater. Chem. Front.*, 2023, **7**, 5447–5454.

